Volatile-consuming reactions fracture rocks and self-accelerate fluid flow in the lithosphere

Masaoki Uno[a,1], Kodai Koyanagawa[a], Hisamu Kasahara[a], Atsushi Okamoto[a], and Noriyoshi Tsuchiya[a]

[a]Graduate School of Environmental Studies, Tohoku University, Sendai 980-8579, Japan

Edited by David Kohlstedt, N. H. Winchell School of Earth Sciences, University of Minnesota, Minneapolis, MN; received June 11, 2021; accepted November 16, 2021

Hydration and carbonation reactions within the Earth cause an increase in solid volume by up to several tens of vol%, which can induce stress and rock fracture. Observations of naturally hydrated and carbonated peridotite suggest that permeability and fluid flow are enhanced by reaction-induced fracturing. However, permeability enhancement during solid-volume–increasing reactions has not been achieved in the laboratory, and the mechanisms of reaction-accelerated fluid flow remain largely unknown. Here, we present experimental evidence of significant permeability enhancement by volume-increasing reactions under confining pressure. The hydromechanical behavior of hydration of sintered periclase [$MgO + H_2O \rightarrow Mg(OH)_2$] depends mainly on the initial pore-fluid connectivity. Permeability increased by three orders of magnitude for low-connectivity samples, whereas it decreased by two orders of magnitude for high-connectivity samples. Permeability enhancement was caused by hierarchical fracturing of the reacting materials, whereas a decrease was associated with homogeneous pore clogging by the reaction products. These behaviors suggest that the fluid flow rate, relative to reaction rate, is the main control on hydromechanical evolution during volume-increasing reactions. We suggest that an extremely high reaction rate and low pore-fluid connectivity lead to local stress perturbations and are essential for reaction-induced fracturing and accelerated fluid flow during hydration/carbonation.

reaction-induced fracturing | reaction-enhanced permeability | volume-increasing reactions | serpentinization | carbonation

Hydration and carbonation reactions in the crust and mantle transport H_2O and CO_2 from Earth's surface to the interior and control volatile budgets within the Earth (1–6). These reactions are characterized by solid-volume increase, by up to several tens of vol%, which induces stress that may lead to fracturing (7–10). The driving force of such stress generation is the thermodynamic free energy released when metastable anhydrous/noncarbonate minerals react with fluids (7). The stress generated by the reaction has the potential to cause rock fracture and fragmentation (7, 11–13), thereby increasing the reactive surface area and fluid flow and further accelerating the reactions (7, 8, 14). Such chemical breaking of rocks, or reaction-induced fracturing, appears to be important in driving hydration and carbonation reactions to completion (8, 15, 16) in an otherwise self-limiting process where reaction products can clog pores and suppress fluid flow, thereby hindering the reaction (15, 17).

Observations of naturally serpentinized and fractured ultramafic rocks indicate a volume increase of 20 to 60% during hydration reactions (13, 18–20), providing evidence of an accelerated supply of fluids during hydration (Fig. 1 *A* and *B*). Natural carbonation of ultramafic rocks is also associated with extensive fracture networks, and reaction-induced fracturing is considered a key process in mineral carbonation (Fig. 1*C*) (7, 8, 21). Numerical simulations indicate a positive feedback between volume-increasing reaction, fracturing, and fluid flow (10, 22–32). Laboratory experiments partially reproduce fracturing during peridotite carbonation, serpentinization, and periclase hydration (29, 33–36); however, hydrothermal flow-through experiments of peridotite serpentinization and carbonation show a decrease in permeability and deceleration of fluid flow and reaction rate (37–42). Observations of the natural carbonation of serpentinized peridotite indicate the decrease in permeability and reduced fluid flow and reaction rate are a consequence of pore clogging related to carbonation (43). Until now, no experimental studies have shown a clear increase in permeability during expansive fluid–rock reactions under confining pressure. As such, despite their geological and environmental importance, the evolution of expansive fluid–rock reactions remains difficult to predict, owing to the complex hydraulic–chemical–mechanical feedbacks underlying these reactions (15, 16, 44). The processes controlling the self-acceleration or deceleration of these reactions remain largely unknown.

Here, we use the hydration of periclase to brucite [$MgO + H_2O \rightarrow Mg(OH)_2$] as an analog for solid-volume–increasing reactions in the Earth. This reaction produces an extreme solid-volume increase of 119%, with a high reaction rate at 100 to 600 °C (45). Previous experimental studies on periclase hydration have revealed that extensive fracturing occurs under certain conditions (29, 33, 35), yet the links between fracturing experiments (periclase hydration), nonfracturing experiments (peridotite hydration/carbonation), and natural observations are unknown. On the basis of in situ observations of fluid flow during the reactions, we clearly show that fluid flow and associated permeability are strongly enhanced by solid-volume–increasing reactions under confining pressure (i.e., at simulated

Significance

Hydration and carbonation are the main reactions that drive volatile cycles in the Earth. These reactions are characterized by a large increase in solid volume, by up to several tens of percent, and may induce fracturing, fluid flow, and further reactions. However, no experimental studies have succeeded in a clear increase in fluid flow during the reactions, and the mechanisms that control acceleration or deceleration remain largely unknown. We present here clear experimental evidence that hydration reactions can fracture rocks and accelerate fluid flow, under confining pressure (i.e., at simulated depth). We conclude that a high reaction rate, relative to the fluid flow rate, is essential for fracturing and accelerated fluid flow during these reactions in the Earth.

Author contributions: M.U. designed research; M.U., K.K., and H.K. performed research; M.U. and A.O. contributed new reagents/analytic tools; M.U. analyzed data; M.U., A.O., and N.T. discussed the experimental results and their implications; and M.U., A.O., and N.T. wrote the paper.

The authors declare no competing interest.

This article is a PNAS Direct Submission.

[1]To whom correspondence may be addressed. Email: uno@geo.kankyo.tohoku.ac.jp.

This article contains supporting information online at http://www.pnas.org/lookup/suppl/doi:10.1073/pnas.2110776118/-/DCSupplemental.

Published January 14, 2022.

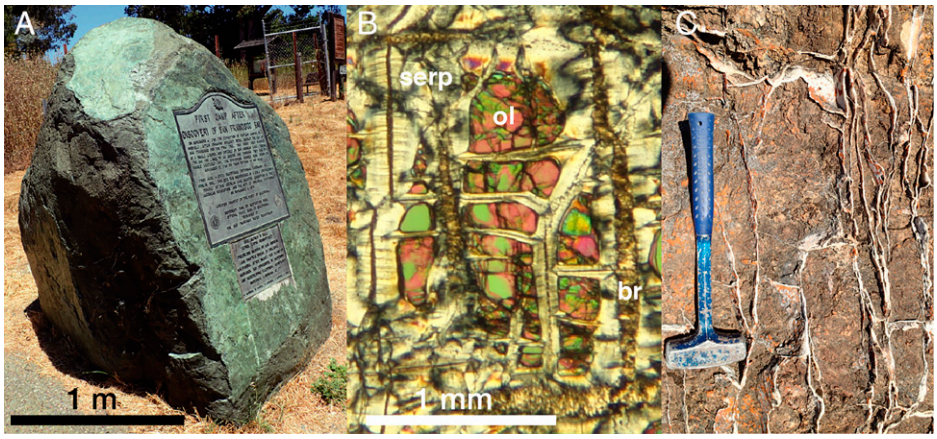

Fig. 1. Reaction-induced fractures related to natural hydration/carbonation. (*A*) Polygonal block of serpentinite cut by planar lizardite veins, extracted from a serpentinite body, San Andreas Lake, California. (*B*) Photomicrograph of mesh structure in partly serpentinized peridotite, Redwood City serpentinite, California [crossed-polarized light (61)]. (*C*) Quartz veins in silica–carbonate rocks (i.e., listvenite, a carbonated ultramafic rock) that occur along the boundaries of serpentinite bodies, San Jose, California. ol, olivine; serp, serpentine (lizardite ± antigorite mixture); br, brucite.

depth). Based on the experimental results and nondimensional parameterization, we propose that the ratio of the initial fluid flow rate to the reaction rate has a primary control on the self-acceleration and deceleration of fluid flow and reactions during hydration and carbonation within the Earth.

Hydrothermal Flow-through Experiments

We conducted hydrothermal flow-through experiments on sintered periclase (MgO) with average grain sizes of 50 to 80 μm (*SI Appendix*, Table S1). To explore the effects of connectivity on the hydromechanical response, sintered periclase samples were prepared with three different initial connected porosities (ϕ_{c0}): ∼19%, 7 to 11%, and <0.1% (Suzuki Rika Co.). These samples were produced by sintering electrofused MgO at 1,000 to 1,500 °C to achieve the designated porosities. The initial porosities were measured using the standard triple weight method (e.g., ref. 46; *SI Appendix*, Table S1). The initial permeabilities (k_0) of these samples were measured under a confining pressure of 20 MPa and room temperature, with the same apparatus as used for the hydrothermal flow-through experiments (*SI Appendix*, Fig. S1), and were $\sim 3 \times 10^{-15}$, 4×10^{-17}, and $<10^{-19}$ m^2, respectively (*SI Appendix*, Table S1). Herein, these MgO sample types are referred to as permeable (P-MgO), moderately permeable (MP-MgO), and impermeable (IP-MgO), respectively. Experiments were conducted at 200 °C and under a confining pressure (P_c) of 20 MPa (*SI Appendix*, Fig. S1). Pore fluid was supplied with a pressure of 5 MPa at the inlet (P_f^{in}), and the outlet back-pressure (P_f^{out}) valve was set to 4, 2, and 3 MPa for P-MgO, MP-MgO, and IP-MgO, respectively (*SI Appendix*, Fig. S1 and Table S1). The outlet end of the sample contained no fluids at the beginning of each experiment. Consequently, the outlet fluid pressure changed with time as fluid flowed through the sample and was monitored by a pressure gauge. The inlet flow rate (Q) was monitored at the syringe pump. Details of the experimental setup are described in *Methods*. The time-sequence data for inlet and outlet pressures, inlet flow rate, and resultant permeability for all the experiments are shown in *SI Appendix*, Fig. S2 and described in detail in *SI Appendix*.

A clear decrease in permeability was observed for P-MgO starting materials during the first ∼100 min of the experiments (Fig. 2*A*). In contrast, IP-MgO sample permeability increased by up to about three orders of magnitude (Fig. 2*B*). The permeability of MP-MgO starting materials showed an initial decrease, by two orders of magnitude, followed by an increase of up to two orders of magnitude (Fig. 2*A*). These experimental results clearly show permeability enhancement during volume-increasing fluid–rock reactions under confining pressure.

X-ray computed tomography (CT) images of the experimental-run products (Fig. 3) show a range of reaction textures. Run products of P-MgO starting materials are uniform in CT values, and reactions proceeded evenly across the thickness of the sample (i.e., in the x–y plane) along the sample length (i.e., the z-axis). Experiments that were stopped at 5 min (FTP08) show a lower reaction extent ($\xi = 0.78$) and higher CT values compared with those stopped at 240 min (FTP06: $\xi = 0.98$); the reaction extent is slightly lower at the outlet end of the sample (FTP08). MP-MgO run products show that reactions proceeded gradually through the sample, from the inlet toward the outlet. The reaction extents and volume change increased with reaction time, from $\xi = 0.03$ and $\Delta V/V_0 = 0.06$ at 3.3 min, to $\xi = 0.94$ and $\Delta V/V_0 = 1.64$ at 30 min. IP-MgO run products show pervasive fracturing close to the inlet in experiments where the reaction extent is lowest (FTD11: $\xi = 0.12$, $\Delta V/V_0 = 0.19$). In experiments with a higher reaction extents, fracturing progressed into the middle of the sample and through to the outlet end of the sample (FTD15 and FTD10). Although the reaction time and reaction extent do not correlate, the reaction extent does show a positive correlation with the final permeability (Fig. 3 and *SI Appendix*, Table S1), highlighting a close relationship between reaction, fracturing, and permeability enhancement.

Microtextures observed in backscattered electron (BSE) images show permeable starting materials are porous and that pores are concentrated on grain boundaries (*SI Appendix*, Fig. S3*A*). P-MgO reacted with H_2O to form brucite along grain boundaries (Fig. 4*A*). Brucite grew in the direction perpendicular to periclase grain boundaries (Fig. 4*B*), with brucite grains maintaining an interstitial porosity (Fig. 4 *B* and *C*).

MP-MgO starting materials are porous along grain boundaries (Fig. 4*D*). For MP-MgO run products with the lowest final permeability (FTMP05: $k_{fin} = 1.1 \times 10^{-18}$ m^2), brucite grew along periclase grain boundaries (Fig. 4*E*). In contrast, MP-MgO run products that exhibited a slight increase in permeability after an initial reduction (FTMP04: $k_{fin} = 7.6 \times 10^{-18}$ m^2) show fragmentation of periclase grains into pieces of size ∼5 to 10 μm (Fig. 4*F*).

IP-MgO starting materials are characterized by closed grain boundaries (*SI Appendix*, Fig. S3). IP-MgO run products are characterized by a hierarchical fragmentation. Domains of periclase aggregates, measuring ∼1 mm, are separated by thick brucite veins (>100 μm in thickness; Fig. 4*I*). Internal to these domains, periclase is further fragmented into zones of aggregates

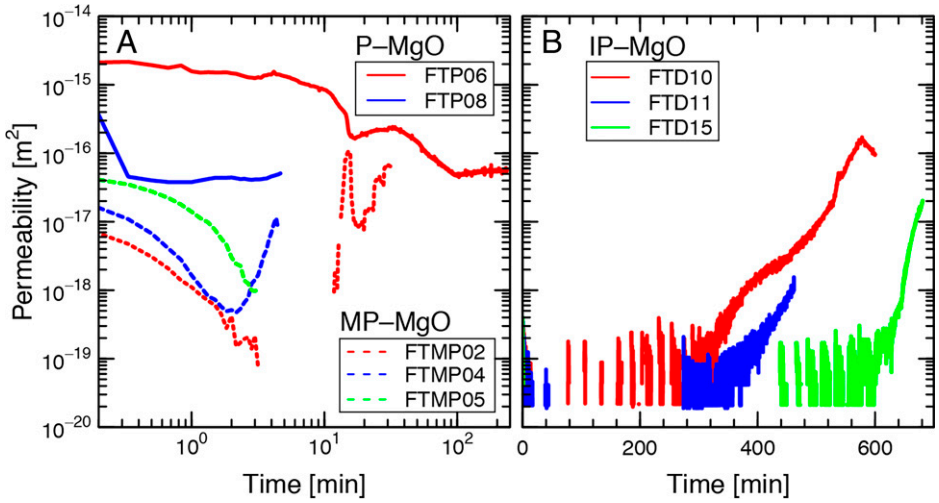

Fig. 2. Evolution of permeability during hydrothermal flow-through experiments. (*A*) Permeable MgO (P-MgO) and moderately permeable MgO (MP-MgO) starting materials. (*B*) Impermeable MgO (IP-MgO) starting materials. Terms beginning with FT indicate experimental run numbers (*SI Appendix*, Table S1).

measuring >100 μm across, separated by thinner brucite veins (>10 μm in thickness). These periclase aggregates are also further fragmented into ~20- to 100-μm grains (Fig. 4 *H* and *I*). Fractures propagated from highly reacted areas into nonreacted materials (Figs. 3*C* and 4*G*) and are filled with brucite that grew perpendicular to the fracture walls.

Processes of Permeability Enhancement

The experimental results indicate that differences in initial permeability of the starting materials played an important role in the textural and permeability evolution during the hydration of sintered periclase. Permeable and moderately permeable samples are characterized by a relatively uniform reaction extents in *x*–*y* sections (Fig. 5 *A* and *B*). In contrast, impermeable samples are characterized by the coexistence of highly reacted and nonreacted zones within a single *x*–*y* section (Fig. 5*C*; i.e., the reaction extents are highly heterogeneous for IP-MgO samples).

To understand the differences in reaction heterogeneity among sample types, the following scale-independent parameters are defined (see *Methods* for full details): 1) the matrix fluid flow rate, Q_{matrix} [/s], is the volumetric H_2O flow rate over the sample volume and 2) the rate of fluid consumption by reaction, Q_{reaction} [/s], is the rate of volumetric H_2O consumption by the hydration reaction, over the sample volume. The ratio $Q_{\mathrm{matrix}}/Q_{\mathrm{reaction}}$ (Ψ) represents the supply rate of H_2O

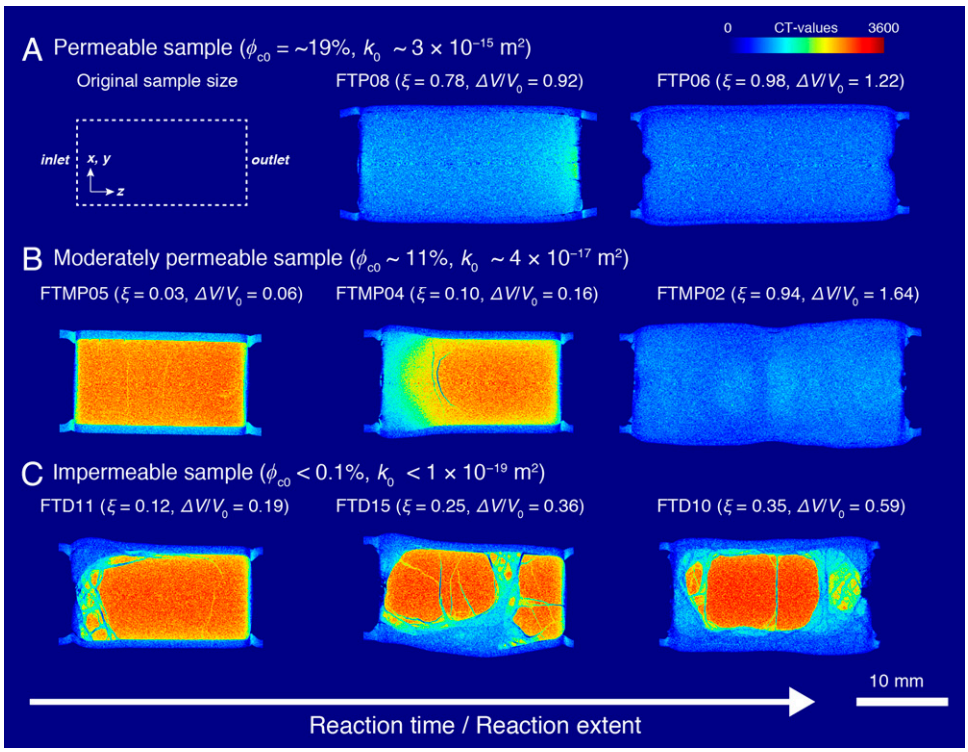

Fig. 3. X-ray CT images of the experimental-run products. ϕ_{c0}, k_0, ξ, and $\Delta V/V_0$ indicate initial connected porosity, initial permeability, reaction extent, and solid volume change relative to the initial sample volume, respectively. Terms beginning with FT are experimental-run numbers (*SI Appendix*, Table S1).

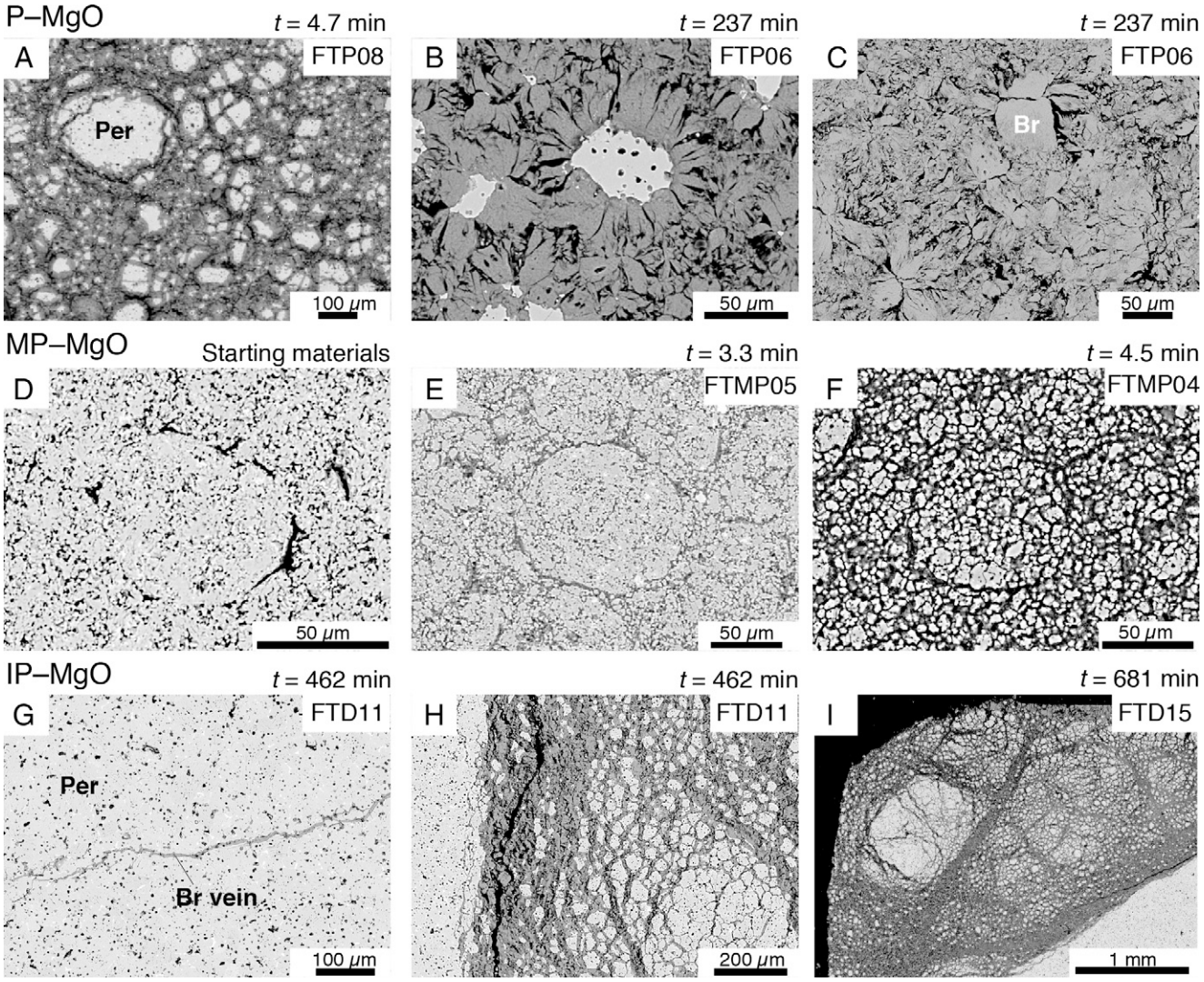

Fig. 4. Microstructures of run products. (*A–C*) BSE images of reactants for permeable MgO starting materials (P-MgO). (*D–F*) Reactants for moderately permeable MgO starting materials (MP-MgO). (*G–I*) Reactants for impermeable MgO starting materials (IP-MgO). Corresponding experimental duration (*t*) is indicated at *Right Top* of each image. Per, periclase; Br, brucite. Terms beginning with FT are experimental-run numbers (*SI Appendix*, Table S1).

relative to the consumption rate of H_2O by reaction. In the case of the starting materials in this study, Ψ-values were 60 to 530, 0.6 to 2.5, and 1 to 4×10^{-2} for the permeable, moderately permeable, and impermeable MgO experiments, respectively. In summary, these Ψ-values indicate that fluid flow front is much faster than reaction in permeable samples, fluid flow front and reaction proceed at similar rates in moderately permeable samples, and fluid flow front is much slower than reaction in impermeable samples. Thus, the textures of the experimental products vary as a function of Ψ and can be interpreted as follows (Fig. 6 *A–C*).

In permeable samples, fluid flow is much faster than the reaction, and fluid fills all the pore space before the reaction begins. Following sample saturation by the pore fluid, the reaction proceeds uniformly throughout the sample. As the reaction extent is uniform at the millimeter scale, samples expand evenly as the reaction proceeds. Consequently, strain gradients across the samples are weak, and no macroscopic fractures are generated (Fig. 6*A*).

In moderately permeable samples, the progression of the fluid flow front is similar to that of the reaction front, and the reaction proceeds gradually as the fluid flows into the sample. As a result, there is a difference in the reaction extent along the sample, from the inlet to the outlet. However, progression of the reaction front is reasonably uniform in the *x–y* plane, resulting in only a minor strain gradient within the sample and the formation of minor macroscopic fractures (Fig. 6*B*).

In impermeable samples, the fluid flow rate is much slower than the reaction rate; hence, fluid is consumed as soon as it reaches the reaction site. Large strain gradients arise between reacted and nonreacted areas because of a variable reaction front at the grain scale. Reacted areas expand and exert tensile stress in adjacent nonreacted areas, leading to the formation of macroscopic fractures. Fluid flow into extension fractures leads to further reaction with periclase to produce brucite. Brucite grows perpendicular to the fracture wall, which induces further expansion, increasing the fracture width and generating tensile stress at the fracture tips that cause fracture propagation (Fig. 6*C*).

Therefore, the ratio of fluid flow rate to fluid consumption rate determines the local position of the reaction front, which controls fracture generation and associated permeability enhancement during hydration (Fig. 6 *A–C*).

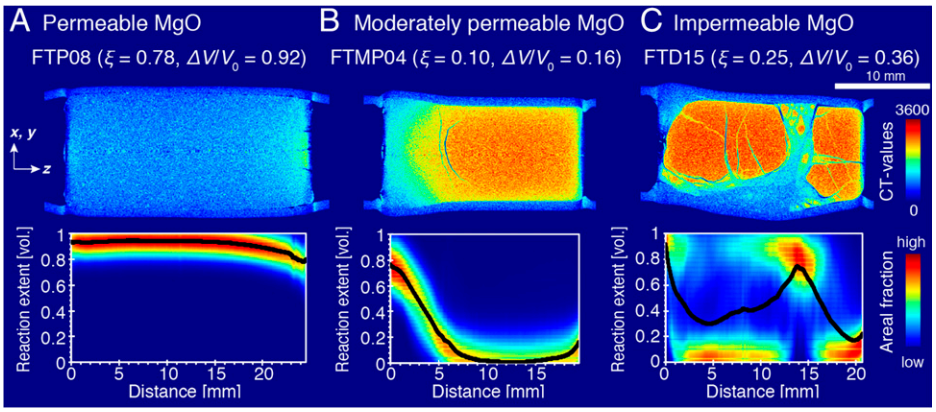

Fig. 5. Profiles of reaction extent along the run products. (*A*) Run products of P-MgO. (*B*) Run products of MP-MgO. (*C*) Run products of IP-MgO. Histograms of volumetric reaction extent for each *x*–*y* section are plotted as a function of distance along the *z*-axis. Terms beginning with FT are experimental-run numbers (*SI Appendix*, Table S1).

Controls on Fracturing and Self-Accelerated Fluid Flow

The above interpretation in the previous section indicates that the nondimensional parameter Ψ (the ratio of fluid flow rate to fluid consumption rate by reaction) controls the hydromechanical behavior of volume-increasing fluid–rock reactions. Shimizu and Okamoto (28) have simulated serpentinization reactions using a discrete element method (DEM), considering elastic strain and failure, fluid flow, and first-order kinetics. They have shown that two parameters determine the textural evolution of serpentinization reactions: 1) the ratio of matrix fluid flow rate to fluid consumption rate (ψ_{matrix}) and 2) the ratio of fracture fluid flow rate to fluid consumption rate ($\psi_{fracture}$). If these two ratios are below unity, surface spallation will occur. When $\psi_{matrix} \leq 1$ (corresponding to $\Psi < 0.02$) and $\psi_{fracture} \geq 10$, extensive polygonal fractures are generated, whereas when $\psi_{matrix} \geq 1{,}000$ (corresponding to $\Psi > 2$), the reaction proceeds diffusionally, and no fractures are generated. Although their ψ_{matrix} is defined for a single DEM particle scale (i.e., 30 to 60 μm), and Ψ for the experimental results in this study are calculated for a macroscopic scale (i.e., the sample size, 10 mm × 20 mm), the relationship between texture and Ψ is largely consistent across DEM results and experimental results (Fig. 6*D*).

In previous studies, permeability measurement during serpentinization and peridotite carbonation (Fig. 6*D*) was conducted for permeable starting materials (i.e., 10^{-15} to 10^{-18} m^2) (37, 38, 40–42) and corresponding to $\Psi = 10^3$ to 10^{10}; hence, the fluid

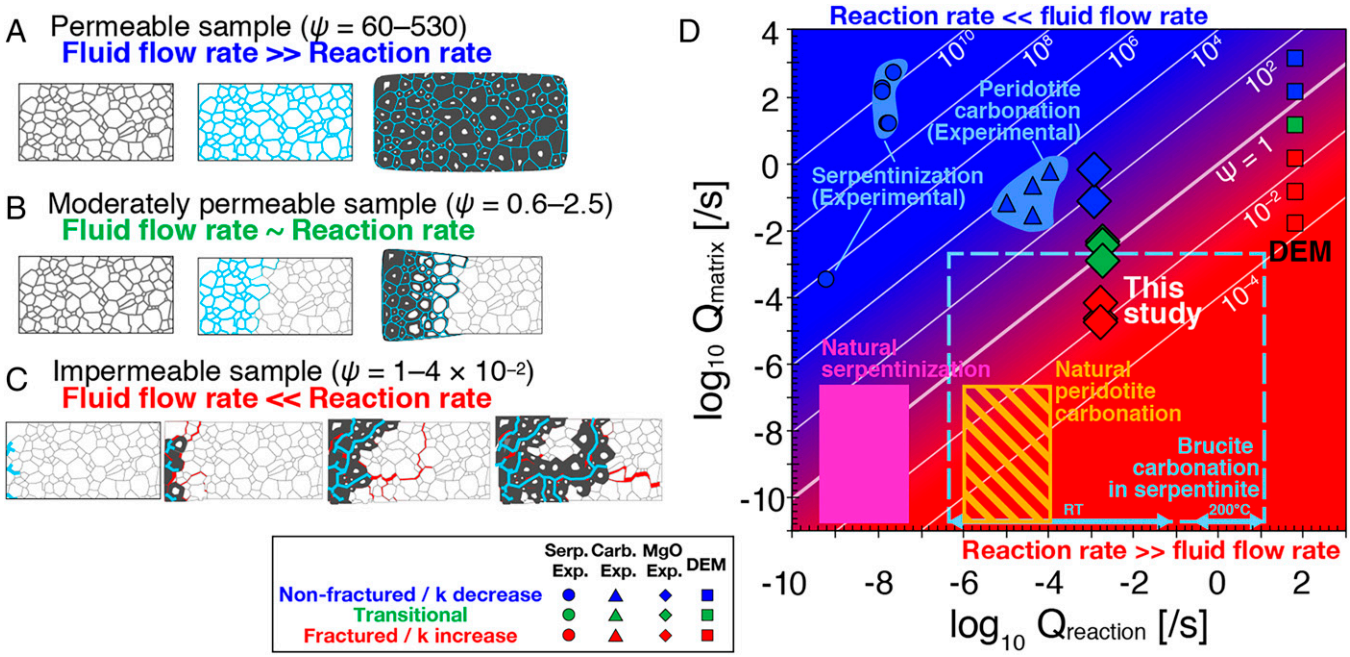

Fig. 6. Influence of fluid flow rate/reaction rate ratio ($\Psi = Q_{matrix}/Q_{reaction}$) on the hydromechanical response to volume-increasing fluid–rock reactions. (*A*–*C*) Schematic model of fluid infiltration and reaction extent in the run products. (*D*) Plot of fluid flow rate (Q_{matrix}) and reaction rate ($Q_{reaction}$) for various volume-increasing fluid–rock reactions, showing the influence of $\Psi = Q_{matrix}/Q_{reaction}$ on the mechanical and hydraulic response. Ranges of natural serpentinization and carbonation are for 280 and 185 °C, respectively, for grain sizes of 0.1 to 10 mm, permeability of 10^{-18} to 10^{-22} m^2, and pressure gradient of 10 MPa/m. Ranges of brucite carbonation are from room temperature (RT) to 200 °C for grain sizes of 0.01 to 0.5 mm, permeability of 10^{-14} to 10^{-22} m^2, and pressure gradient of 10 MPa/m. Data sources: serpentinization (experimental), refs. 41 and 42; peridotite carbonation (experimental), refs. 37, 38, and 40; natural serpentinization, natural peridotite carbonation, and brucite carbonation (reaction rate from ref. 53, ref. 54) fitted by ref. 52, and refs. 59 and 60; permeability of intact peridotite and serpentinite from refs. 38 and 41 and ref. 63; and DEM, ref. 28.

flow rate was much higher than the reaction rate. These experiments are characterized by a reduction in permeability during hydration/carbonation reactions and are consistent with the interpretation that a high fluid flow rate relative to the reaction rate will result in pore clogging.

In contrast to these experiments, the permeability of natural, intact peridotite is usually as low as 10^{-18} to 10^{-22} m^2 at the scale of a core sample (e.g., refs. 12, 38, and 41). At the field scale (i.e., bore hole measurements), the permeability of ultramafic bodies are 10^{-14} to 10^{-15} m^2 (47–49) and is controlled mainly by macroscopic fissures (50). Such fissures would serve as system boundaries along which fluid would have easy access. The access of fluid to unreacted grains is controlled predominantly by the grain-scale permeability (10^{-18} to 10^{-22} m^2). With a spatial scale of >1 m (i.e., the size of the intact peridotite body or blocks separated by fissures) and a fluid pressure difference of ∼10 MPa across the margin of the peridotite blocks [i.e., fluid pressure difference between fissures and unreacted grains inside the intact rocks (14, 51)], the value of Q_{matrix} in natural intact peridotite is $<10^{-7}$/s. Note that if the size of the system is larger and/or the fluid pressure difference is lower, Q_{matrix} will be lower. Given the typical reaction rate of serpentinization and peridotite carbonation at 280 and 185 °C (52–54), with a typical grain size of 0.1 to 10 mm, $Q_{reaction}$ for natural serpentinization and peridotite carbonation is 4.5×10^{-8} to 10^{-10}/s and 1.0×10^{-4} to 10^{-6}/s, with $\Psi = 4 \times 10^{-4}$ to 10^{2} and 2.0×10^{-7} to 0.2, respectively; i.e., the lower Q_{matrix} part of natural serpentinization and most of natural peridotite carbonation are falling within the condition of reaction rate ≫ fluid flow rate (Fig. 6*D*). Therefore, the observation that natural serpentinization and peridotite carbonation accompany fracturing is explained by a low fluid supply rate compared with the reaction rate in intact peridotite.

Carbonation of serpentinite is also a solid-volume–increasing reaction under a closed system except for H_2O and CO_2 (e.g., refs. 55 and 56). Although carbonation reactions of serpentine minerals are known to occur at a similar rate to, or slower than, those of olivine at laboratory experiments (e.g., refs. 57 and 58), carbonation of brucite is much faster at temperatures from room temperature to 200 °C (e.g., refs. 58–60). Assuming that the typical grain size of brucite in serpentinite is 10 to 500 μm (e.g., refs. 61 and 62), $Q_{reaction}$ for brucite carbonation ranges from 4.0×10^{-7}/s (room temperature, atmospheric CO_2) to 12 (200 °C, P_{CO2} = 1 MPa). As the permeability of intact serpentinite is typically on the order of 10^{-14} to 10^{-22} m^2 at the scale of a core sample (63), the Ψ-value of brucite carbonation ranges from 5×10^{3} to 10^{-12}, which indicates fracturing for most conditions (Fig. 6*D*). Moreover, brucite typically occurs as vein networks in mesh structures within serpentinite (Fig. 1*B*), and such a heterogeneous distribution of reactive minerals would further promote fracturing by enhancing local stress perturbation, as demonstrated by previous experimental studies and numerical simulations on periclase-calcite/serpentine aggregates (29, 35) and troctolite (7, 10, 24). In any case, the rapid nature of brucite carbonation reactions indicates fracturing would occur over a wide range of temperatures (Fig. 6*D*).

Based on the relationship between $Q_{reaction}$ and Q_{matrix}, natural serpentinization has similar Ψ-values to IP-MgO in this study (Fig. 6*D*). The polygonal blocks of the remaining periclase in these experiments (IP-MgO in Figs. 3*C* and 4*I* and *SI Appendix*, Fig. S4) are surrounded by brucite veins and are similar to polygonal blocks formed during natural serpentinization that are surrounded by lizardite veins (Fig. 1*A*) (61). Similar polygonal blocks are commonly observed in weathered dolerite (25, 64) and leucite replaced by analcime (25). At smaller scales, the partly reacted IP-MgO shows fragmented periclase grains surrounded by brucite that grew perpendicular to grain boundaries (Fig. 4 *B* and *H* and *SI Appendix*, Fig. S4*B*), which are very similar to the commonly observed mesh structure of serpentinite (Fig. 1*B*). The similarities in texture between IP-MgO reaction products and natural serpentinites and other volume-increasing fluid–rock reaction products suggest that Ψ has a primary control on textural evolution during such fluid–rock reactions.

Based on the similarity of Ψ in our experiments with values calculated for natural serpentinization, we posit that the permeability of peridotite would increase from 10^{-19} m^2 (corresponding to $\Psi = 0.4$ at 280 °C, for a grain size of ∼100 μm) to 10^{-16} m^2 during natural serpentinization reactions, an increase of three orders of magnitude. Such high permeability during serpentinization is consistent with the permeability required for hydrothermal circulation [i.e., $>10^{-18}$ m^2 (e.g., refs. 65 and 66)] that likely occurs at some slow-spreading ridges (67). As the serpentinization reactions are usually rate limited by the supply of fluids (14), such permeability enhancement would facilitate a marked acceleration in the hydration of the oceanic lithosphere.

The results of this study show that the balance between the rate of fluid supply by fluid flow and rate of fluid consumption by reaction is a primary control on the mechanical and hydraulic evolution of rocks during volume-increasing fluid–rock reactions. We have experimentally demonstrated that permeability is clearly enhanced by volume-increasing fluid–rock reactions under confining pressure and that fluid flow can be self-accelerated during hydration and carbonation reactions. Subject to the appropriate environmental conditions (i.e., fluid supply and deformation) and ratio of fluid flow to reaction rate ($\Psi < 1$), such self-acceleration could enhance initially inert hydration or carbonation reactions by more than three orders of magnitude, thereby promoting a marked acceleration of mineral hydration and carbonation. This could significantly facilitate downward volatile transport from Earth's surface and the hydrothermal advection of fluids in the crust and mantle.

Our results give insight into the conditions necessary to accelerate hydration of the oceanic mantle lithosphere (24), which has a strong influence on the H_2O budget on Earth (1, 4), as well as conditions for accelerated carbonation reactions of ultramafic rocks that would enhance mineral carbonation and storage (8). The results may also be applied to inhibit damage caused by the swelling of anhydrite during tunnel construction and geothermal developments (68) and to understand the weakening of plate boundary faults by the swelling of smectite (69). Yet, the mechanical and hydraulic responses to volume-increasing fluid–rock reactions are much more complex in nature than currently addressed numerically or through experimentation, as they involve the coupled processes of fluid flow–reaction–deformation–solute transport (15–19, 22–33, 36, 70–72). The heterogeneous distribution of reactive minerals may enhance stress perturbations and further affects these feedbacks (7, 10, 24, 29, 35). This study used homogeneous starting materials, and explored conditions under which the reaction rate and/or fluid flow rate are high enough that deformation and solute transport are negligible. Further studies on the coupling of deformation and solute transport with fluid flow and reaction, from the μm to field scales, are needed to fully understand the effects of complex hydraulic–chemical–mechanical feedbacks on volume-increasing fluid–rock reactions.

Methods

Hydrothermal Flow-through Experiments. Hydrothermal flow-through experiments were conducted using a hydrothermal flow-through apparatus comprising a syringe pump (73) and a customized sample assembly (*SI Appendix*, Fig. S1). The inlet fluid pressure was maintained at a constant pressure using the syringe pump, and the outlet fluid pressure was regulated by a back-pressure valve. The confining pressure was applied via an independent pump, using distilled water. The inlet flow rate was monitored by the syringe pump, and the inlet fluid pressure, outlet fluid pressure, and confining pressure were monitored using independent pressure gauges. The temperature was regulated by a heater housed within the apparatus pressure vessel and was

monitored by thermocouples attached to the inlet and outlet of the sample assembly.

A cylindrical, sintered MgO sample (Suzuki Sci. Co.; 10 mm in diameter and 20 mm in length) was enclosed in a tubular Teflon jacket and placed between two spacers, each with a 2-mm-diameter hole to allow fluid through-flow (*SI Appendix*, Fig. S1*B*). The inlet end of the sample assembly was connected to a 1/16″ stainless steel pipe to allow application of confining pressure along the length of the sample (the sample *z*-axis).

After placing the sample assembly within the pressure vessel, the apparatus was pressurized to a confining pressure of 20 MPa and heated to 200 °C. The MgO sample was kept dry during heating. After reaching 200 °C, the experiment was started by opening the inlet valve, allowing fluid to flow into the sample at a constant pressure. It is important to note that the outlet end of the sample contained no fluids at the beginning of each experiment.

Permeability was measured by applying Darcy's law using the monitored inlet flow rate and inlet and outlet pressures. The viscosity of H_2O was derived using the monitored inlet pressure and temperature, from pressure- and temperature-dependent calibration (74) (i.e., 1.35×10^{-4} Pa s at 5 MPa and 200 °C).

Experiments were stopped at a designated reaction time by releasing the inlet and outlet fluid pressure and then cooling the sample assembly via circulation of the confining fluids. Confining pressure was released after cooling the sample assembly. Samples were dried at room temperature overnight and further dried in an oven at 90 °C for several hours.

Permeability of the starting materials was determined by independent experiments conducted with same confining pressure (20 MPa) at room temperature with same inlet pressure as the reacting experiments (*SI Appendix*, Table S1).

Analyses of Experimental-Run Products. Samples were weighed before and after experiments to determine the reaction extent (ξ). The experimental-run products were imaged using X-ray CT, subjected to thermogravimetric (TG) analysis, and prepared as thin sections for observation via optical microscopy and electron microprobe. Reaction extent by mass balance (ξ_{MB}) was calculated from the mass change between starting materials (m_{st}) and run products (m_{rp}), divided by the theoretical mass increase for complete hydration ($\xi_{MB} = \frac{(m_{rp} - m_{st})}{18.0/40.3\, m_{st}}$).

X-ray CT analysis of the run products was conducted using a microfocus X-ray CT scanner (Comscantecno ScanXmate-D225RSS270) at the Graduate School of Environmental Studies, Tohoku University, Sendai, Japan. The X-ray tube voltage and current were set to 120 kV and 150 μA, respectively, giving an X-ray spot size of ∼9 μm. The resulting pixel matrix was 1,856 × 1,472, and the voxel size varied from 18 to 24 μm/px depending on the size of the analyzed run product. Reaction extent by X-ray CT (ξ_{CT}) was obtained from the CT values in *x*–*y* sections, using the average CT values of the starting materials (∼2,750, ∼2,520, and ∼2,180 for IP-MgO, MP-MgO, and P-MgO, respectively) and those of completely reacted run products (∼780).

Run products with relatively uniform reaction extent (P-MgO and MP-MgO starting materials) were cut along the sample length for TG analysis. Approximately 500 mg run product was ground to powder, and ∼20-mg portions were set in platinum pods. The samples were analyzed using a thermogravimetry (Rigaku Thermo Plus EVOII TG8120). Samples were heated from room temperature to 1,050 °C at a rate of 10 °C per min. Temperatures were kept constant at 105 and 1,050 °C for 10 min. Loss on ignition (LOI) was obtained in the temperature range 105 to 1,050 °C to exclude the loss of mass associated with molecular water on the powder surface. Reaction extent by TG analysis (ξ_{TG}) was calculated as the LOI divided by the theoretical H_2O content in brucite (i.e., 31.0 wt.%).

The volumes of starting materials and run products (V_0 and V_1) were determined by X-ray CT images by integrating the cross-sectional area of sample at each *x*–*y* scan. The volume change was determined as $\Delta V/V_0 = (V_1 - V_0)/V_0$ (*SI Appendix*, Table S1).

Definition of Q_{matrix} and $Q_{reaction}$. The following scale-independent parameters are considered:

$$\text{Matrix fluid flow rate } [/s] : Q_{matrix} = \frac{q_{sample}}{AL} = \frac{k_0 \Delta P}{\mu L^2}, \quad [1]$$

$$\text{Fluid consumption rate by reaction } [/s] : Q_{reaction} = \frac{S_{sample} v(P,T)}{AL} \frac{V_{H2O}}{V_{per}}, \quad [2]$$

where Q_{matrix} indicates the volumetric H_2O flow rate over the sample volume, and $Q_{reaction}$ is the volumetric H_2O consumption rate by the hydration reaction over the sample volume. q_{sample} is the volumetric H_2O flow rate, k_0 is the permeability of the sample, ΔP is the initial fluid pressure difference between the sample surface and dry pore space, S_{sample} is the surface area of the reactant, $v(P, T)$ is the reaction front velocity as a function of pressure (P) and temperature (T), A and L are the cross-sectional area and length of the sample, respectively, and V_{H2O} and V_{per} are molar volumes of H_2O and periclase, respectively. The ratio $Q_{matrix}/Q_{reaction}$ is denoted as Ψ and represents the supply rate of H_2O compared with the consumption rate of H_2O by the reactions. It is noted that the second term of Eq. **1** ($Q_{matrix} = \frac{k_0 \Delta P}{\mu L^2}$) have been used for application of Eq. **1** to natural data and DEM results.

For each experimental condition, k_0 was taken as the obtained initial permeability (*SI Appendix*, Fig. S1), ΔP is set as the inlet fluid pressure (i.e., 5 MPa), S_{sample} was derived from the surface area of the sample assuming a spherical grain size of 79, 50, and 56 μm for P-MgO, MP-MgO, and IP-MgO (*SI Appendix*, Table S1), and $v(P, T)$ was derived from the experimental calibration (29). The actual size of the cylindrical sample employed as a starting material was used for A and L.

Permeability of natural intact peridotite and serpentinite measured in laboratory are in the ranges of 10^{-18} to 10^{-22} m^2 (12, 38, 41) and 10^{-14} to 10^{-22} m^2 (63), respectively. Contrary, field-scale permeability may be larger for partly serpentinized peridotite in Oman ophiolite [i.e., 10^{-14} to 10^{-15} m^2 (47, 48)], which are mainly controlled by macroscopic fissures (50). As fluid access to each grain is controlled by grain-scale permeability, we adopt laboratory permeability rather than field-scale permeability for the calculation of Q_{matrix} for natural serpentinization and peridotite carbonation (10^{-18} to 10^{-22} m^2 for peridotite) and carbonation of brucite in serpentinite (10^{-14} to 10^{-22} m^2 for serpentinite).

ΔP values for natural serpentinization, peridotite carbonation, and brucite carbonation are assumed as ∼10 MPa (i.e., fluid pressure difference between the fissures and unreacted grains inside the intact rocks). Note that equilibrium H_2O vapor pressures during olivine serpentinization is as low as 0.2 MPa at 180 °C (14). Therefore, the fluid pressure on unreacted olivine grain surfaces is negligible (i.e., <0.2 MPa) compared to those in water filled fissures. An assumption of fluid pressure in fissures on the order of ∼10 MPa corresponds to a highly permeable fissure network extending unobstructed for more than 1 km or to water in fissures at lithostatic pressure at a depth greater than ∼300 m.

The ψ_{matrix} parameter, defined in previous DEM results (28), relates to the scale of the DEM particles. This is different from the definition of Ψ in this study; hence, Ψ from DEM results (28) was recalculated based on Eqs. 1 and 2 (Fig. 6*D*).

Data Availability. All study data are included in the article and/or *SI Appendix*.

ACKNOWLEDGMENTS. This study was financially supported in part by JSPS (Japan Society for the Promotion of Science) KAKENHI Grant Nos. JP15H01136 and JP17H05310 awarded to M.U., JP17H02981 awarded to A.O. and M.U., and JP16H06347 and JP18KK0376 awarded to A.O., and by JST/JICA (Japan Science and Technology Agency / Japan International Cooperation Agency) SATREPS (Science and Technology Research Partnership for Sustainable Development) Grant No. JPMJSA1703 awarded to N.T., A.O., and M.U. M.U. thanks S. Kirby for helping with a field survey and S. Kirby and R.G. Coleman for discussions on the occurrences of serpentinite and carbonated ultramafic rocks.

1. L. H. Rüpke, J. P. Morgan, M. Hort, J. A. D. Connolly, Serpentine and the subduction zone water cycle. *Earth Planet. Sci. Lett.* **223**, 17–34 (2004).
2. R. Dasgupta, M. M. Hirschmann, The deep carbon cycle and melting in Earth's interior. *Earth Planet. Sci. Lett.* **298**, 1–13 (2010).
3. E. M. Stewart *et al.*, Carbonation and decarbonation reactions: Implications for planetary habitability. *Am. Mineral.* **104**, 1369–1380 (2019).
4. B. R. Hacker, H_2O subduction beyond arcs. *Geochem. Geophys. Geosyst.* **9**, Q03001 (2008).
5. P. B. Kelemen, C. E. Manning, Reevaluating carbon fluxes in subduction zones, what goes down, mostly comes up. *Proc. Natl. Acad. Sci. U.S.A.* **112**, E3997–E4006 (2015).
6. T. Plank, C. E. Manning, Subducting carbon. *Nature* **574**, 343–352 (2019).
7. P. B. Kelemen, G. Hirth, Reaction-driven cracking during retrograde metamorphism: Olivine hydration and carbonation. *Earth Planet. Sci. Lett.* **345–348**, 81–89 (2012).
8. P. B. Kelemen *et al.*, Rates and mechanisms of mineral carbonation in peridotite: Natural processes and recipes for enhanced, in situ CO_2 capture and storage. *Annu. Rev. Earth Planet. Sci.* **39**, 545–576 (2011).
9. J. F. Rudge, P. B. Kelemen, M. Spiegelman, A simple model of reaction-induced cracking applied to serpentinization and carbonation of peridotite. *Earth Planet. Sci. Lett.* **291**, 215–227 (2010).
10. B. Jamtveit, A. Malthe-Sørenssen, O. Kostenko, Reaction enhanced permeability during retrogressive metamorphism. *Earth Planet. Sci. Lett.* **267**, 620–627 (2008).
11. T. K. T. Wolterbeek, R. van Noort, C. J. Spiers, Reaction-driven casing expansion: Potential for wellbore leakage mitigation. *Acta Geotechnol.* **13**, 341–366 (2018).
12. R. van Noort, T. K. T. Wolterbeek, M. R. Drury, M. T. Kandianis, C. J. Spiers, The force of crystallization and fracture propagation during in-situ carbonation of peridotite. *Minerals (Basel)* **7**, 1–31 (2017).

13. O. Plümper, A. Røyne, A. Magrasó, B. Jamtveit, The interface-scale mechanism of reaction-induced fracturing during serpentinization. *Geology* **40**, 1103–1106 (2012).
14. A. H. MacDonald, W. S. Fyfe, Rate of serpentinization in seafloor environments. *Tectonophysics* **116**, 123–135 (1985).
15. F. Renard, Reaction-induced fracturing: When chemistry breaks rocks. *J. Geophys. Res. Solid Earth* **126**, e2020JB021451 (2021).
16. B. Malvoisin, Y. Y. Podladchikov, A. V. Myasnikov, Achieving complete reaction while the solid volume increases: A numerical model applied to serpentinisation. *Earth Planet. Sci. Lett.* **563**, 116859 (2021).
17. M. Andreani *et al.*, Experimental study of carbon sequestration reactions controlled by the percolation of CO_2-rich brine through peridotites. *Environ. Sci. Technol.* **43**, 1226–1231 (2009).
18. B. Malvoisin, C. Zhang, O. Müntener, L. P. Baumgartner, P. B. Kelemen, Measurement of volume change and mass transfer during serpentinization: Insights from the Oman Drilling Project. *J. Geophys. Res. Solid Earth* **125**, 1–17 (2020).
19. B. Malvoisin, Mass transfer in the oceanic lithosphere: Serpentinization is not isochemical. *Earth Planet. Sci. Lett.* **430**, 75–85 (2015).
20. J. C. de Obeso, P. B. Kelemen, Fluid rock interactions on residual mantle peridotites overlain by shallow oceanic limestones: Insights from Wadi Fins, Sultanate of Oman. *Chem. Geol.* **498**, 139–149 (2018).
21. J. M. Matter, P. B. Kelemen, Permanent storage of carbon dioxide in geological reservoirs by mineral carbonation. *Nat. Geosci.* **2**, 837–841 (2009).
22. A. Malthe-Sørenssen, B. Jamtveit, P. Meakin, Fracture patterns generated by diffusion controlled volume changing reactions. *Phys. Rev. Lett.* **96**, 245501 (2006).
23. O. Evans, M. Spiegelman, P. B. Kelemen, Phase-field modeling of reaction-driven cracking: Determining conditions for extensive olivine serpentinization. *J. Geophys. Res. Solid Earth* **125**, 1–21 (2020).
24. K. Yoshida, A. Okamoto, H. Shimizu, R. Oyanagi, N. Tsuchiya, Fluid infiltration through oceanic lower crust in response to reaction-induced fracturing: Insights from serpentinized troctolite and numerical Models. *J. Geophys. Res. Solid Earth* **125**, e2020JB020268 (2020).
25. B. Jamtveit, C. V. Putnis, A. Malthe-Sørenssen, Reaction induced fracturing during replacement processes. *Contrib. Mineral. Petrol.* **157**, 127–133 (2009).
26. O. I. Ulven, H. Storheim, H. Austrheim, A. Malthe-Sørenssen, Fracture initiation during volume increasing reactions in rocks and applications for CO_2 sequestration. *Earth Planet. Sci. Lett.* **389**, 132–142 (2014).
27. A. Okamoto, H. Shimizu, Contrasting fracture patterns induced by volume-increasing and -decreasing reactions: Implications for the progress of metamorphic reactions. *Earth Planet. Sci. Lett.* **417**, 9–18 (2015).
28. H. Shimizu, A. Okamoto, The roles of fluid transport and surface reaction in reaction-induced fracturing, with implications for the development of mesh textures in serpentinites. *Contrib. Mineral. Petrol.* **171**, 1–18 (2016).
29. H. Kuleci, O. I. Ulven, E. Rybacki, B. Wunder, R. Abart, Reaction-induced fracturing in a hot pressed calcite-periclase aggregate. *J. Struct. Geol.* **94**, 116–135 (2017).
30. O. I. Ulven, A. Beinlich, J. Hövelmann, H. Austrheim, B. Jamtveit, Subarctic physicochemical weathering of serpentinized peridotite. *Earth Planet. Sci. Lett.* **468**, 11–26 (2017).
31. O. Evans, M. Spiegelman, P. B. Kelemen, A poroelastic model of serpentinization: Exploring the interplay between rheology, surface energy, reaction, and fluid flow. *J. Geophys. Res. Solid Earth* **123**, 8653–8675 (2018).
32. L. Zhang *et al.*, Modeling porosity evolution throughout reaction-induced fracturing in rocks with implications for serpentinization. *J. Geophys. Res. Solid Earth* **124**, 5708–5733 (2019).
33. X. Zheng, B. Cordonnier, W. Zhu, F. Renard, B. Jamtveit, Effects of confinement on reaction-induced fracturing during hydration of periclase. *Geochem. Geophys. Geosyst.* **19**, 2661–2672 (2018).
34. W. Zhu *et al.*, Experimental evidence of reaction-induced fracturing during olivine carbonation. *Geophys. Res. Lett.* **43**, 9535–9543 (2016).
35. X. Zheng *et al.*, Mixed-mode strain localization generated by hydration reaction at crustal conditions. *J. Geophys. Res. Solid Earth* **124**, 4507–4522 (2019).
36. F. Klein, V. Le Roux, Quantifying the volume increase and chemical exchange during serpentinization. *Geology* **48**, 552–556 (2020).
37. S. Peuble *et al.*, Multi-scale characterization of the incipient carbonation of peridotite. *Chem. Geol.* **476**, 150–160 (2018).
38. H. Lisabeth, W. Zhu, P. B. Kelemen, A. Ilgen, Experimental evidence for chemo-mechanical coupling during carbon mineralization in ultramafic rocks. *Earth Planet. Sci. Lett.* **474**, 355–367 (2017).
39. J. Hövelmann, H. Austrheim, B. Jamtveit, Microstructure and porosity evolution during experimental carbonation of a natural peridotite. *Chem. Geol.* **334**, 254–265 (2012).
40. S. Peuble *et al.*, CO_2 geological storage in olivine rich basaltic aquifers: New insights from reactive-percolation experiments. *Appl. Geochem.* **52**, 174–190 (2015).
41. A. Farough, D. E. Moore, D. A. Lockner, R. P. Lowell, Evolution of fracture permeability of ultramafic rocks undergoing serpentinization at hydrothermal conditions: An experimental study. *Geochem. Geophys. Geosyst.* **17**, 44–55 (2016).
42. M. Godard, L. Luquot, M. Andreani, P. Gouze, Incipient hydration of mantle lithosphere at ridges: A reactive-percolation experiment. *Earth Planet. Sci. Lett.* **371–372**, 92–102 (2013).
43. N. Jöns, W. A. Kahl, W. Bach, Reaction-induced porosity and onset of low-temperature carbonation in abyssal peridotites: Insights from 3D high-resolution microtomography. *Lithos* **268–271**, 274–284 (2017).
44. R. M. Skarbek, H. M. Savage, P. B. Kelemen, D. Yancopoulos, Competition between crystallization-induced expansion and creep compaction during gypsum formation, and implications for serpentinization. *J. Geophys. Res. Solid Earth* **123**, 5372–5393 (2018).
45. H. Kuleci, C. Schmidt, E. Rybacki, E. Petrishcheva, R. Abart, Hydration of periclase at 350°C to 620°C and 200 MPa: Experimental calibration of reaction rate. *Mineral. Petrol.* **110**, 1–10 (2016).
46. F. A. L. Dullien, *Porous Media: Fluid Transport and Pore Structure*, 2nd ed. (Academic Press, 1991).
47. B. Dewandel, P. Lachassagne, A. Qatan, Spatial measurements of stream baseflow, a relevant method for aquifer characterization and permeability evaluation. Application to a hard-rock aquifer, the Oman ophiolite. *Hydrol. Processes* **18**, 3391–3400 (2004).
48. G. Lods, D. Roubinet, J. M. Matter, R. Leprovost, P. Gouze, Groundwater flow characterization of an ophiolitic hard-rock aquifer from cross-borehole multi-level hydraulic experiments. *J. Hydrol. (Amst.)* **589**, 125152 (2020).
49. J. Jeanpert *et al.*, Fracture controlled permeability of ultramafic basement aquifers. Inferences from the Koniambo massif, New Caledonia. *Eng. Geol.* **256**, 67–83 (2019).
50. B. Dewandel *et al.*, A conceptual hydrogeological model of ophiolite hard-rock aquifers in Oman based on a multiscale and a multidisciplinary approach. *Hydrogeol. J.* **13**, 708–726 (2005).
51. K. Hatakeyama, I. Katayama, K. I. Hirauchi, K. Michibayashi, Mantle hydration along outer-rise faults inferred from serpentinite permeability. *Sci. Rep.* **7**, 13870 (2017).
52. P. B. Kelemen, J. Matter, In situ carbonation of peridotite for CO_2 storage. *Proc. Natl. Acad. Sci. U.S.A.* **105**, 17295–17300 (2008).
53. H. M. Lamadrid, Z. Zajacz, F. Klein, R. J. Bodnar, Synthetic fluid inclusions XXIII. Effect of temperature and fluid composition on rates of serpentinization of olivine. *Geochim. Cosmochim. Acta* **292**, 285–308 (2021).
54. W. K. O'Connor *et al.*, Aqueous mineral carbonation: Mineral availability, pretreatment, reaction parametrics, and process studies. *U.S. Dep. Energy Final Rep.* DOE/ARC-TR-04-002 (2005).
55. L. D. Hansen, G. M. Dipple, T. M. Gordon, D. A. Kellett, Carbonated serpentinite (listwanite) at Atlin, British Columbia: A geological analogue to carbon dioxide sequestration. *Can. Mineral.* **43**, 225–239 (2005).
56. P. B. Kelemen *et al.*, *Mass Transfer into the Leading Edge of the Mantle Wedge: Initial Results from Oman Drilling Project Hole BT1B* (Earth Sp. Sci. Open Arch, 2021).
57. S. J. Gerdemann, W. K. O'Connor, D. C. Dahlin, L. R. Penner, H. Rush, Ex situ aqueous mineral carbonation. *Environ. Sci. Technol.* **41**, 2587–2593 (2007).
58. P. B. Kelemen *et al.*, Engineered carbon mineralization in ultramafic rocks for CO_2 removal from air: Review and new insights. *Chem. Geol.* **550**, 119628 (2020).
59. A. L. Harrison, I. M. Power, G. M. Dipple, Accelerated carbonation of brucite in mine tailings for carbon sequestration. *Environ. Sci. Technol.* **47**, 126–134 (2013).
60. K. J. Fricker, A. H. A. Park, Effect of H_2O on $Mg(OH)_2$ carbonation pathways for combined CO_2 capture and storage. *Chem. Eng. Sci.* **100**, 332–341 (2013).
61. M. Uno, S. Kirby, Evidence for multiple stages of serpentinization from the mantle through the crust in the Redwood City Serpentinite mélange along the San Andreas Fault in California. *Lithos* **334–335**, 276–292 (2019).
62. A. Miyoshi, T. Kogiso, N. Ishikawa, K. Mibe, Role of silica for the progress of serpentinization reactions: Constraints from successive changes in mineralogical textures of serpentinites from Iwanaidake ultramafic body, Japan. *Am. Mineral.* **99**, 1035–1044 (2014).
63. I. Katayama *et al.*, Permeability profiles across the crust-mantle sections in the Oman Drilling Project inferred from dry and wet resistivity data. *J. Geophys. Res. Solid Earth*, **125**, e2019JB018698 (2020).
64. A. Røyne, B. Jamtveit, J. Mathiesen, A. Malthe-Sørenssen, Controls on rock weathering rates by reaction-induced hierarchical fracturing. *Earth Planet. Sci. Lett.* **275**, 364–369 (2008).
65. R. B. Hanson, The hydrodynamics of contact metamorphism. *Geol. Soc. Am. Bull.* **107**, 595–611 (1995).
66. C. E. Manning, S. E. Ingebritsen, Permeability of the continental crust: Implications of geothermal data and metamorphic systems. *Rev. Geophys.* **37**, 127–150 (1999).
67. R. P. Lowell, P. A. Rona, Seafloor hydrothermal systems driven by the serpentinization of peridotite. *Geophys. Res. Lett.* **29**, 26–1–26-4 (2002).
68. C. Butscher, T. Mutschler, P. Blum, Swelling of clay-sulfate rocks: A review of processes and controls. *Rock Mech. Rock Eng.* **49**, 1533–1549 (2016).
69. J. Kameda *et al.*, Fault weakening caused by smectite swelling. *Earth Planets Space* **71**, 131 (2019).
70. B. Jamtveit, H. Austrheim, A. Malthe-Sørenssen, Accelerated hydration of the Earth's deep crust induced by stress perturbations. *Nature* **408**, 75–78 (2000).
71. M. G. Guren *et al.*, Molecular dynamics study of confined water in the periclase-brucite system under conditions of reaction-induced fracturing. *Geochim. Cosmochim. Acta* **294**, 13–27 (2021).
72. A. Okamoto *et al.*, Rupture of wet mantle wedge by self-promoting carbonation. *Commun. Earth Environ.* **2**, 151 (2021).
73. A. Okamoto, H. Takana, N. Watanabe, H. Saishu, N. Tsuchiya, Fluid pocket generation in response to heterogeneous reactivity of a rock fracture under hydrothermal conditions. *Geophys. Res. Lett.* **44**, 10306–10315 (2017).
74. E. R. Likhachev, Dependence of water viscosity on temperature and pressure. *Tech. Phys.* **48**, 514–515 (2003).